An update to this article is included at the end

Fire Safety Journal 164 (2026) 104897

Contents lists available at ScienceDirect

Fire Safety Journal

journal homepage: www.elsevier.com/locate/firesaf

Sample-form-induced transport effects in the micro-scale decomposition of PMMA

Felix Armbrust [a,*], Tristan Hehnen [b], Jochen Zehfuß [a], Olaf Riese [a], Lukas Arnold [b,c]

[a] Institute of Building Materials, Concrete Construction and Fire Safety, Fire Research Center, Technische Universität Braunschweig, Beethovenstraße 52, 38106 Braunschweig, Germany

[b] Chair of Computational Civil Engineering, University of Wuppertal, Pauluskirchstraße 7, 42285 Wuppertal, Germany

[c] Institute for Advanced Simulation, Forschungszentrum Jülich, Wilhelm-Johnen-Straße, 52428 Jülich, Germany

ARTICLE INFO

Dataset link: https://doi.org/10.24355/dbbs.084-202606100939-0

Keywords:
Polymethylmethacrylate
Thermal analysis
0D-assumption
Pyrolysis modelling
Kinetic analysis
Fire spread prediction

ABSTRACT

Kinetic models for thermal decomposition of combustible materials are fundamental for predicting fire growth and flame spread. Kinetic parameters are typically derived from micro-scale experiments, assuming data are free from transport phenomena (the 0D-assumption). Different specimen forms can yield distinct decomposition behaviours, as observed for polymethylmethacrylate (PMMA), yet origins and implications for fire spread modelling remain uninvestigated. To address this gap, powder specimens of varying particle sizes and piece specimens of black cast PMMA were analysed using simultaneous thermal analysis, evolved gas analysis, morphological characterisation, and gel permeation chromatography. Results indicate that specimen-form-dependent differences are attributable to mass transport restrictions rather than heat transfer limitations, material alterations, or changes in decomposition chemistry. This conclusion required investigations beyond standard guidelines, as mass down-scaling alone would have implied the absence of transport limitations. In the low-temperature region, diffusion-limited gas release through the solid matrix dominates, whilst during the main decomposition peak the regime shifts to convective bubble transport, dependent on sample mass. Kinetic analysis confirmed derived parameters are implicitly influenced by transport effects, with direct consequences for fire spread predictions. Preliminary observations for other materials suggest specimen-form-dependent influences are not unique to PMMA, underlining the broader relevance for the fire science community.

1. Introduction

For predictions of fire growth and flame spread, fire models rely on a set of interconnected sub-models that represent the key physical and chemical processes governing fire behaviour. Their predictive capability remains limited, because the coupling between gas-phase combustion and condensed-phase decomposition is still insufficiently resolved and the parametrisation of the underlying sub-models remains a major source of uncertainty [1].

Part of this uncertainty is linked to the treatment of the condensed phase. Material models play an important role, as they describe the thermal decomposition of the condensed material, which controls the release of volatiles that feed gas-phase combustion and may also support direct reactions within the condensed phase (e.g. oxidation). To describe the relevant condensed phase processes, these models must include relevant transport processes like mass and energy transfer together with a suitable kinetic description of decomposition.

In general, the decomposition kinetics are described by the reaction rate equation ($\mathrm{d}\alpha/\mathrm{d}t$) [2]:

$$\frac{\mathrm{d}\alpha}{\mathrm{d}t} = k(T)\ f(\alpha)\ h(p) \tag{1}$$

Here, α denotes the degree of conversion and thus the progress of the reaction, defined for mass-loss processes as $\alpha(t) = (m_\mathrm{i} - m(t))/(m_\mathrm{i} - m_\infty)$. In this expression, $m(t)$ is the instantaneous sample mass, m_i the initial mass and m_∞ the final residual mass obtained after the reaction concluded.

The rate constant is given by $k(T)$, while $f(\alpha)$ defines the reaction model. A pressure-dependent term $h(p)$ may also be included, although it is often neglected in practice ($h(p) = 1$) [2]. Various formulations for the reaction model exist in the literature, whereas the temperature dependence of the rate constant is typically described by an Arrhenius expression

* Corresponding author.
E-mail addresses: felix.armbrust1@tu-braunschweig.de (F. Armbrust), hehnen@uni-wuppertal.de (T. Hehnen), j.zehfuss@tu-braunschweig.de (J. Zehfuß), o.riese@tu-braunschweig.de (O. Riese), l.arnold@fz-juelich.de (L. Arnold).

https://doi.org/10.1016/j.firesaf.2026.104897
Received 2 February 2026; Received in revised form 26 May 2026; Accepted 5 June 2026
Available online 16 June 2026
0379-7112/© 2026 The Authors. Published by Elsevier Ltd. This is an open access article under the CC BY license (http://creativecommons.org/licenses/by/4.0/).

$$k(T) = A\ \exp\left(-\frac{E}{R\,T}\right) \tag{2}$$

where A denotes the pre-exponential factor, E the activation energy and R the universal gas constant [2,3]. The experimentally determined activation energy is often referred to as the apparent activation energy (E_a). In addition, it is sometimes reported in a conversion-dependent form ($E_{a,\alpha}$). The parameters A, E and the reaction model $f(\alpha)$ are commonly referred to as the kinetic triplet, as they constitute the essential quantities that must be specified for a kinetic description [4]. In real materials, thermal decomposition often proceeds in several steps, with reactions occurring in parallel and/or consecutively and possibly also interdependently [5]. In such cases, both, the specification of the dependencies between the individual decomposition steps and the increased number of kinetic parameters for each step can make the kinetic description considerably more challenging.

To determine the kinetic parameters, experimental data describing the physical quantity of interest are required, for example data obtained from thermogravimetric analysis (TGA), differential scanning calorimetry (DSC) or micro-scale combustion calorimetry (MCC) [6–8]. These experiments rely on the fundamental assumption that the process is independent of any transport phenomena, so that the measured data reflect only the intrinsic kinetics, the so-called 0D-assumption. Since micro-scale experiments are influenced by a wide range of factors, various experimental boundary conditions must be specified carefully. Key examples include the type of purge gas and the purge-gas flow rate, the physical form of the sample (e.g. piece or powder), the sample mass and the heating rate. The latter two can lead to relevant transport processes due to thermal inertia and thus alter the apparent reaction behaviour. Additional influences arise from the choice of crucible and other experimental details. Moreover, adequate calibration of the instrument is essential to ensure the reliability and comparability of the data. An overview of the most relevant aspects is provided in the ICTAC recommendations [3] and further guidance can be found in the respective standards [6–8].

There is, to some extent, freedom in how micro-scale experiments may be conducted, particularly with regard to the physical form of the investigated specimen. The standards require that the test specimen must be representative of the sample to be examined [6–8]. While this definition may be widely accepted within the field of thermal analysis, it lacks a clear and unambiguous interpretation in fire science, where a broad range of specimen geometries is commonly employed, e.g. [9–15].

To illustrate this ambiguity, consider the simulation of flame spread over a polymethylmethacrylate (PMMA) sheet: whilst the most physically representative specimen would, in principle, be a solid PMMA piece, some authors advocate the use of powdered samples, for example as a general strategy to avoid distortion arising from heat-transport limitations [16].

That the choice of specimen form can influence the observed decomposition behaviour is, in itself, an established finding – yet its implications extend well beyond the micro-scale. In previous work [17], kinetic parameters derived from micro-scale experiments on both PMMA powder and PMMA pieces were used to simulate flame spread and the resulting discrepancies at the micro-scale level were shown to propagate into significant variations in the predicted flame-spread rate – findings that are further supported by the theoretical analysis of Quaresma et al. [18]. Despite its direct relevance to fire spread predictions, no consensus exists within the fire science community on which specimen form is appropriate for kinetic parameter derivation and the physical reasons underlying specimen-form-dependent decomposition behaviour remain unresolved.

DiDomizio and McKinnon demonstrated that the duration of cryo-milling applied to PMMA substantially influences its decomposition behaviour: longer milling times, corresponding to smaller particle sizes, increase the proportion of reactions occurring at lower temperatures. Crucially, no such effect was observed for polyvinylchloride (PVC) under identical conditions [19], suggesting that the underlying mechanisms are material-specific and cannot therefore be resolved by general experimental guidelines alone, but must be investigated for each material individually. A conclusive explanation for the observed differences was not provided. This is further corroborated by Oswald and Wiedemann [20], who showed that particle size governs not only the onset temperature of thermally induced dehydration in cobalt hydroxy-sulphate hydrates (85–310 °C across 0.3–250 μm), but also the controlling mechanism itself — shifting from nucleation-dominated kinetics for small particles to diffusion-controlled behaviour for larger ones. Taken together, these findings demonstrate that specimen-form effects cannot be reduced to a single, universal cause. Whilst heat-transport limitations are frequently invoked, the underlying physico-chemical mechanisms may differ substantially between materials. It is therefore not sufficient to assume that powdering a specimen inherently satisfies the 0D-assumption. Rather, the origins of any specimen-form-dependent behaviour must be investigated explicitly.

The causes of specimen-form-dependent decomposition behaviour can be manifold, each requiring a distinct response. If the differences arise from heat or mass transfer limitations that violate the 0D-assumption, the experimental procedure must be adapted by reducing the sample mass or adjusting the heating rate until transport-free conditions are achieved. If the underlying causes are of a mechanistic nature, as demonstrated for example by Oswald and Wiedemann [20], either the kinetic model must be extended to capture the relevant mechanisms, or the specimen form must be selected such that its governing transport processes reflect those of the application scenario of interest. If the differences are attributable to material alterations introduced by the specimen preparation process such as changes in molar mass distribution or micro-structure, the preparation procedure itself must be revised to avoid these structural modifications. Identifying and addressing the correct cause is therefore a prerequisite for deriving reliable kinetic parameters, as failure to do so risks introducing systematic errors into the pyrolysis model that may ultimately compromise the accuracy of fire spread predictions.

Specimen-form-dependent decomposition behaviour of black cast PMMA had already been established in prior work [17]. In a complementary preliminary investigation, this effect was further screened for four additional polymeric and lignocellulosic materials — pine wood (PW), polystyrene (PS), polyvinyl chloride (PVC) and polyurethane (PU). The results demonstrated that such effects are material-dependent, with PW and PU exhibiting systematic differences between specimen forms (Figs. A.1 and A.2), whilst PS and PVC (Figs. A.3 and A.4) showed no discernible influence. This suggests that specimen-form effects may be relevant for a range of materials of practical interest to the fire science community, warranting careful consideration in the derivation of kinetic parameters for pyrolysis modelling. The present study therefore aims to examine the underlying causes of the observed behaviour for black cast PMMA in detail.

To this end, black cast PMMA powder specimens of varying particle sizes and PMMA piece specimens – all derived from the same sheet material – were investigated by means of simultaneous thermal analysis (STA), with the resulting data for selected specimen forms subsequently employed in a formal kinetic analysis to examine how the derived kinetic parameters vary with particle size. Complementary Fourier-Transform Infrared Spectroscopy (FTIR) and morphological characterisation were conducted to provide further insight into the observed differences in decomposition behaviour. Since it could not be excluded that the powder production process alters the molar mass distribution of the material, gel permeation chromatography (GPC) measurements were additionally carried out, motivated by the findings of Ferriol et al. [21], who reported differences in the decomposition behaviour of cast and extruded PMMA and attributed these to the considerably higher molar mass characteristic of cast PMMA. The specific objectives of this study are therefore: (i) to identify the physico-chemical mechanisms responsible for the distinct decomposition behaviour observed between powder and piece specimens of black cast PMMA and (ii) to assess how the choice of specimen form affects the derived kinetic parameters.

Table 1
Sample forms and size specifications examined.

Sample	Size
Powder 1	<63 μm
Powder 2	63–80 μm
Powder 3	80–112 μm
Powder 4	112–200 μm
Powder 5	200–300 μm
Powder 6	300–400 μm
Powder 7	400–500 μm
Powder 8	>500 μm
Piece	≈1 mm

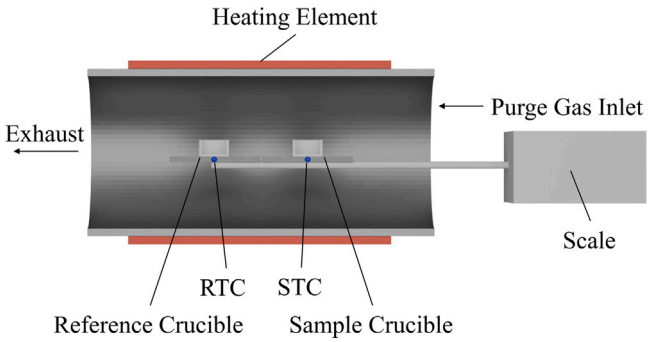

Fig. 1. Schematic representation of the horizontally supported STA setup, showing the reference thermocouple (RTC) measuring T_r and the sample thermocouple (STC) measuring T_s.

2. Material and methods

2.1. Material and sample preparation

PMMA was chosen as the sample material because it exhibits a decomposition behaviour of moderate complexity, even though it decomposes in a multi-step process [21–23]. The specific material examined was a black cast PMMA, commercially available as Plexiglas GS black 9H01 by Röhm.

To produce the powders, small pieces were cut from the sheet using a side cutter and subsequently subjected to a milling process with an ultra-centrifugal mill (ZM 200, Retsch). Before each milling step, the material was cooled for several minutes in a liquid-nitrogen bath to prevent any unintended thermal influence during the milling process that might alter the material. Different sieve sizes (0.5–1.5 mm) and rotor speeds (10,000–18,000 rpm) were employed for the grinding process. In total, five successive milling stages were carried out and after each stage a fraction of the powder was taken to obtain different particle-size fractions.

Subsequently, a vibratory sieve shaker (AS 200, Retsch) equipped with different sieves was used to obtain different particle-size fractions. Table 1 summarises all sample forms examined in the experimental study presented here, comprising eight powder fractions and the piece samples.

Various samples were prepared for the different experiments, each adjusted to a nominal mass (m_0; deviations: ±10% of the nominal value; measurement uncertainty: ±0.01 mg). While the required amount of powder could be weighed directly, one or two small pieces were typically selected for the piece experiments to achieve the nominal mass. All samples were conditioned in accordance with ISO 291 (standard climate: 23 ± 2 °C, 50 ± 10% RH) and stored in a desiccator for at least one week.

2.2. Simultaneous thermal analysis

A horizontally supported STA device (TGA/DSC 3+, Mettler Toledo) was employed to characterise the thermally induced decomposition behaviour of the PMMA samples, see Fig. 1. The instrument is equipped with a differential thermal analysis (DTA) sensor, enabling the derivation of the heat flow ($\dot{Q}$) from the temperature difference between the reference (T_r) and the sample temperature (T_s). Mass (m) and temperature (T) are recorded simultaneously over time, allowing the derivation of thermogravimetric (TG; $m(T)$ or $m(t)$) and derivative thermogravimetric (dTG; $\mathrm{d}m/\mathrm{d}t$) data. As the analysis is primarily concerned with characterising the decomposition behaviour, the sample mass is considered the principal quantity of interest.

As the overarching objective of the study was to investigate the causes of sample form-dependent changes in decomposition behaviour, particular care was taken to ensure the validity of the 0D-assumption. To this end, the recommendations of the ICTAC kinetics committee [3] were taken into account and, beyond these, a comprehensive preliminary assessment – both theoretical and experimental – was undertaken, as detailed in the following subsection. For the selection of an appropriate maximum sample mass, initial sample masses (m_0) of 8, 4, 2, 1 and 0.5 mg were investigated.

After an appropriate sample mass had been established, non-isothermal STA experiments were carried out at constant heating rates (β) of 3, 5, 10, 20 and 30 K min^{-1}. The temperature programme ranged from an initial temperature of 30 °C to a final temperature of 700 °C. Employing several heating rates is beneficial in multiple respects. It is essential for investigating the individual steps of a multi-step decomposition process and verifying their independence [3]. Moreover, the reliable determination of kinetic parameters typically necessitates a minimum of three to five temperature programmes [2].

Since isothermal experiments can provide insight into the reaction model ($f(\alpha)$ in Eq. (1)), experiments at an isothermal temperature of 300 °C were carried out for each sample form. Including at least one isothermal run alongside multiple constant-heating-rate experiments is considered best practice for identifying the underlying reaction mechanism and determining the kinetic triplets [2].

Following the recommendation in [3], a standard purge-gas flow rate of 100 cm^3 min^{-1} was employed. All measurements were carried out in an inert nitrogen atmosphere, with a 15-minute pre-purge implemented before each run to ensure inert conditions [6]. To verify whether the 15-minute pre-purge phase is sufficient to establish an inert atmosphere, preliminary measurements of the oxygen concentration were conducted (Fig. A.5). The TGA furnace was deliberately opened and subsequently closed to mimic a typical sample loading procedure. This step represents the primary moment at which ambient air can enter the furnace and alter the internal atmosphere. Following this perturbation, the oxygen concentration was monitored for 15 min. As observed, the brief opening of the furnace does not result in atmospheric oxygen levels. The concentration decreases to below 0.1 vol% within less than 100 s, indicating that the applied purge duration is sufficient to re-establish an inert atmosphere.

Prior to the experimental series, mass and temperature calibrations were performed for each experimental boundary condition following the applicable standards [6,7]. The balance calibration was conducted via an internal function of the device and indium, aluminium and zinc were used to calibrate temperature and heat flow. Blank curves were subtracted to compensate for buoyancy effects. All measurements were performed in 70 mm^3 alumina crucibles with an outer height-to-diameter ratio of 0.75. The STA is installed on a vibration-isolation platform to maximise signal quality.

To ensure reliable and high-quality data, all standard non-isothermal (β = const.) and isothermal measurements were repeated three times. For all subsequent analyses, only the measured sample temperature was used and the results were evaluated with respect to the normalised mass (m/m_0).

2.3. Evaluation of transport limitations

To investigate the influence of particle size on potential transport processes, the validity of the 0D-assumption was assessed at both the particle and sample scale using a combination of theoretical and experimental approaches. This analysis served a dual purpose: first, to evaluate the extent to which transport phenomena may affect the observed decomposition behaviour across different particle size fractions and second, to define an appropriate maximum sample mass for all subsequent micro-scale experiments.

2.3.1. Biot and fourier numbers

Internal heat transfer limitations were evaluated using the dimensionless Biot (Bi) and Fourier (Fo) numbers. Both criteria must be satisfied simultaneously to justify the assumption that each particle behaves as a spatially isothermal body whose temperature follows the imposed heating ramp without delay.

The Biot number quantifies the ratio of external heat transfer resistance to internal conductive resistance. Values of $\mathrm{Bi} < 0.1$ indicate thermally thin behaviour, confirming the absence of significant intraparticle temperature gradients:

$$\mathrm{Bi} = \frac{h_{\mathrm{eff}} L_{\mathrm{c}}}{\lambda} \tag{3}$$

where h_{eff} is the effective heat transfer coefficient, L_{c} is the characteristic length of the particle (for a sphere of radius (r): $L_{\mathrm{c}} = r/3$) and λ is the thermal conductivity of the material.

The effective heat transfer coefficient accounts for conductive, convective and radiative contributions:

$$h_{\mathrm{eff}} = h_{\mathrm{cond}} + h_{\mathrm{conv}} + h_{\mathrm{rad}} \tag{4}$$

Below 800 ° C and under typical TGA operating conditions, heat transfer is predominantly governed by conduction [3,24]. Radiative contributions are therefore neglected. Conduction itself may occur via two pathways: (i) direct thermal contact between the particles and the crucible base and (ii) conduction through the surrounding purge gas. The former is considered negligible, as the low sample mass and the surface roughness of the alumina crucible limit the effective contact area and thus contact conductance. Heat transfer is therefore assumed to occur primarily through the latter pathway, namely conduction through the nitrogen atmosphere. Since the nitrogen purge gas flow may also give rise to convective heat transfer, this mode was additionally included in the analysis to ensure a conservative upper-bound estimate.

The effective heat transfer coefficient was estimated using a Nusselt-number-based approach:

$$h_{\mathrm{eff}} = \frac{\mathrm{Nu}\,\lambda_{\mathrm{fluid}}}{d_{\mathrm{p}}} \tag{5}$$

with the Nusselt number determined from the Ranz–Marshall correlation [25]:

$$\mathrm{Nu} = 2 + 0.6 \left(\frac{\rho_{\mathrm{fluid}}\, v\, d_{\mathrm{p}}}{\mu} \right)^{1/2} \left(\frac{c_{\mathrm{p,fluid}}\, \mu}{\lambda_{\mathrm{fluid}}} \right)^{1/3} \tag{6}$$

where d_{p} is the particle diameter, λ_{fluid} the thermal conductivity of the fluid, ρ_{fluid} the fluid density, μ the dynamic viscosity and v the velocity of the surrounding fluid. Two limiting cases were considered: (i) pure conduction ($\mathrm{Nu} = 2$) and (ii) full convective influence of the purge gas flow. Although the Ranz–Marshall correlation was derived for freely exposed particles in external flow – conditions not strictly met in TGA due to crucible shielding – its application here yields a conservative overestimate of convective heat transfer.

The Fourier number assesses the temporal response of the particle temperature to the imposed heating ramp. It represents the ratio of the thermal diffusion timescale to the characteristic experimental timescale:

$$\mathrm{Fo} = \frac{\alpha_{\mathrm{th}}\, t}{L_{\mathrm{c}}^2} \tag{7}$$

where $\alpha_{\mathrm{th}} = \lambda/(\rho c_{\mathrm{p}})$ is the thermal diffusivity. The characteristic time t was defined as the inverse of the peak reaction rate, evaluated at the DTG peak temperature T_{p}:

$$t = \frac{1}{\mathrm{d}\alpha/\mathrm{d}t\big|_{\mathrm{peak}}} = \frac{R T_{\mathrm{p}}^2}{\beta E_{\mathrm{a}}} \tag{8}$$

Using the estimate of the peak reaction rate from [26], the characteristic reaction timescale is obtained as its inverse, providing a conservative estimate for the Fourier number evaluation.

High Fourier numbers ($\mathrm{Fo} > 1$) confirm that intraparticle heat conduction is sufficiently fast for the particle temperature to closely follow the imposed heating ramp. Should both criteria be satisfied simultaneously ($\mathrm{Bi} < 0.1$ and $\mathrm{Fo} > 1$), intra-particle heat transfer limitations can be considered negligible and the 0D-assumption is justified across all particle sizes investigated in this study.

2.3.2. Evaluation of temperature discrepancies for molten PMMA

The particle-scale analysis above assumes that individual particles retain their shape throughout the experiment and do not interact with one another. For PMMA, a thermoplastic material, this assumption holds only until the onset of melting. Once molten, a particle-based treatment is no longer applicable.

For the molten state, a methodology following the approach of Snegirev et al. [27] was employed to assess potential discrepancies between the measured and the actual sample temperature. Within this framework, two contributions to a potential temperature delay were considered, namely a thermal lag (ΔT_1) and a temperature depression associated with endothermic decomposition (ΔT_2).

The thermal lag arises from heat diffusion through the melt layer and the crucible bottom before reaching the temperature sensor:

$$\Delta T_1 = \beta(\tau_{\mathrm{m}} + \tau_{\mathrm{c}}) = \beta \left(\frac{(\delta_{\mathrm{m}}/2)^2}{2\,\alpha_{\mathrm{th,m}}} + \frac{(\delta_{\mathrm{c}}/2)^2}{2\,\alpha_{\mathrm{th,c}}} \right) \tag{9}$$

where τ_{m} and τ_{c} are the thermal time constants of the melt layer and crucible bottom, respectively. δ_{m} and δ_{c} are the corresponding layer thicknesses and $\alpha_{\mathrm{th,m}}$, $\alpha_{\mathrm{th,c}}$ their respective thermal diffusivities.

The temperature deviation caused by heat consumption during decomposition is approximated as:

$$\Delta T_2 \approx \frac{\rho_{\mathrm{m}}\, \Delta h_{\mathrm{g}}\, \beta E_{\mathrm{a}}/(R T_{\mathrm{p}}^2)}{n\, \lambda_{\mathrm{m}}} \left(\frac{\delta_{\mathrm{m}}}{2} \right)^2 \tag{10}$$

where ρ_{m} is the melt density, Δh_{g} the heat of gasification, n the shape parameter and λ_{m} the thermal conductivity of the melt. Both ΔT_1 and ΔT_2 were quantified across the full range of sample masses used in this study.

2.3.3. Mass down-scaling

While the preceding theoretical analyses, conducted at both particle and sample scales, provide a consistent framework for assessing potential heat transfer limitations, they are inherently based on simplifying assumptions. As with other analytical estimates reported in the literature (e.g. [28]), such approaches cannot fully capture the complexity of real samples, particularly with respect to intra- and inter-particle interactions as well as instrument-specific influences.

Moreover, the theoretical considerations presented above are restricted to heat transfer phenomena and do not account for potential mass transport limitations, which may become relevant during decomposition, especially in the presence of evolving gaseous species.

For these reasons, an experimental verification of the transport regime is indispensable. Following the recommendations of ICTAC [3], a mass down-scaling approach was therefore applied to systematically evaluate and minimise both heat and mass transfer limitations. This method involves progressively reducing the sample mass at the maximum heating rate until congruent conversion curves are obtained, indicating transport-independent behaviour. The highest sample mass fulfilling this criterion is subsequently defined as the maximum admissible mass for the kinetic experiments.

In the present study, nominal masses of 8, 4, 2, 1 and 0.5 mg were investigated at a heating rate of 30 K min^{-1}. The finest (powder 1) and coarsest powder fraction (powder 8), as well as the piece samples, were selected to span the range of potential intra- and inter-particle transport effects.

2.4. Gel permeation chromatography

Gel permeation chromatography (GPC) was employed to determine the molar-mass distribution of the nine different sample forms. The samples were dissolved in tetrahydrofuran (THF) for a minimum of two days under continuous magnetic stirring to ensure complete dissolution. Prior to injection, all solutions were passed through a 5 μm PTFE syringe filter to remove any remaining particulates. The measurements were conducted in accordance with OECD test guideline 118, where applicable [29].

GPC measurements were performed on a system equipped with a Shodex RI-71 refractive index detector. Separation was achieved using a set of MZ-Gel SDplus columns with a nominal pore size of 10.6 nm (8 mm × 600 mm, 10 μm), specifically designed for the characterisation of high-molar-mass polymers. THF was used as the mobile phase at a constant flow rate of 1 $cm^3 min^{-1}$ and a column temperature of 20 °C. The sample solutions had a concentration of approximately 3 mg cm^{-3} and an injection volume of 25 mm^3 was applied. Toluene was added as an internal standard to monitor retention-time stability.

The system was calibrated using a series of polystyrene (PS) standards spanning a molar-mass range of 682 to 1,670,000 g mol^{-1} and the calibration function was fitted using a polynomial model.

In addition to information on the molar-mass (M) distribution, GPC also provides information on the number-average molar mass (M_n^*), the weight-average molar mass (M_w^*) and dispersity (Đ) of the samples.

As the calibration was based on PS standards, all reported quantities represent apparent values. This does not affect the interpretation in the present context, as the analysis focuses on the relative differences between the PMMA sample forms rather than absolute molar-mass accuracy.

2.5. Evolved gas analysis

To obtain deeper mechanistic insight into the decomposition behaviour, selected STA experiments were complemented by evolved-gas analysis using Fourier-transform infrared (FTIR) spectroscopy (Nicolet iS5, Thermo Fisher Scientific). FTIR spectra were recorded in the range from 400 to 4000 cm^{-1}. As the measurements were performed online, chemigrams for specific wavelength regions could be derived. These show the temporal evolution of the IR intensity within a selected spectral interval.

The system also enabled comparison of the recorded spectra with calibration data from NIST, allowing identification of released components. To avoid condensation of the evolving gases, the entire transfer line and measurement system were maintained at 250 °C throughout the analysis.

2.6. Analysis of external structure

To investigate the external morphology of different sample forms at defined temperatures, STA experiments were interrupted at predetermined temperature levels and the samples were rapidly removed for photographic documentation. Images were captured at discrete stages of the thermal decomposition to visualise the evolution of the sample morphology.

The finest powder (powder 1), the coarsest powder (powder 8) and the piece form were examined at 23 (room temperature), 320 and 370 °C. Within the applied heating programme (β = 30 K min^{-1}), 320 °C corresponds to the shoulder preceding the main decomposition step, whereas 370 °C falls within the main decomposition peak.

To ensure that all samples experienced identical thermal conditions, separate experiments were conducted for the photographs taken at elevated temperatures. Consequently, the samples imaged at 320 and 370 °C do not correspond to the same individual specimens.

2.7. Kinetic analysis

The comprehensive STA dataset was used for a detailed kinetic analysis, aiming to elucidate how the physical form of the sample affects the derived kinetic parameters, and ultimately, the modelling of the decomposition reaction.

The different heating rates were employed to examine whether interdependencies exist between the individual steps of the multi-step decomposition [3]. In addition, the data served as the basis for an isoconversional analysis. For this, the Kissinger–Akahira–Sunose (KAS) method was applied, using the implementation provided in the Python package FireSciPy, which includes the Starink approximation [30,31].

Finally, the isothermal experiments provided insights that allowed conclusions to be drawn regarding the dominant reaction model [2].

To demonstrate the practical consequences of specimen-form-dependent variations in kinetic parameters, fire spread simulation results from prior work [17] were drawn upon, illustrating how differences in the derived parameters propagate into fire spread predictions.

3. Results

3.1. Theoretical analysis of heat transfer limitations

To assess the potential presence of heat transfer limitations, particle-size-based estimates were carried out using the Biot and Fourier numbers. Unless stated otherwise, all parameters required for these calculations are provided in Table A.1. Temperature dependencies of these parameters were neglected, which can be justified for approximative estimates of this kind.

The particles were assumed to be spherical for the calculation of the dimensionless numbers. The characteristic length (L_c) was thus taken as one third of the particle radius (r_p), where the radius was determined assuming that particles within each size fraction have a mean diameter (d_p) corresponding to the midpoint of the respective fraction boundaries (see Table 1).

The Biot number was evaluated according to Eqs. (3), (5) and (6) for two limiting cases. In the first case, only conductive heat transfer was considered by setting the flow velocity to $v = 0$, consistent with the established finding that conduction dominates heat transfer in TGA below 800 °C [3,24]. In the second case, the particles were assumed to be directly exposed to the nitrogen purge gas flow, representing a conservative upper bound: forced convection enhances external heat transfer and thus increases the Biot number. The corresponding flow velocity was estimated from the purge gas flow rate and the furnace geometry, yielding $v = 5.31 \cdot 10^{-3}$ m s^{-1} for the present setup.

For the conduction-only case, the Biot number is Bi = 0.077 for all particle sizes. When convection is additionally considered, the values increase slightly with particle size, ranging from 0.079 to 0.083 (Table A.2). In both cases Bi < 0.1, confirming that no significant intra-particle temperature gradients should arise under the experimental conditions and that the particle temperature can be approximated as spatially uniform.

The Fourier number was calculated according to Eq. (7) using an apparent activation energy of 200 kJ mol^{-1} (derived as an estimate from [21]) and a dTG peak temperature of 380 °C (derived from own data). The maximum heating rate applied in this study (β = 30 K min^{-1}) was used to obtain a conservative estimate of the characteristic time. The resulting Fo values range from 139 for the piece sample to 34,944 for the finest powder fraction (Table A.3), with values increasing as particle size decreases. Since Fo ≫ 1 in all cases, heat diffusion within the particles proceeds much faster than the decomposition reaction,

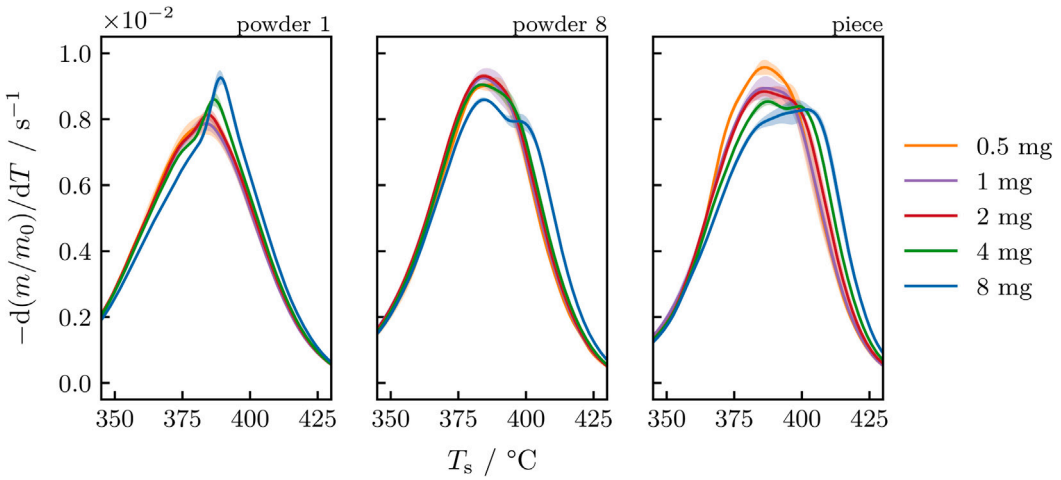

Fig. 2. dTG signal comparison for the mass down-scaling. Focus is on the main decomposition peak of powder 1, powder 8 and the piece sample at $\beta = 30$ K min^{-1} (solid lines: average; shaded areas: standard deviation).

confirming that intraparticle heat transfer limitations can be excluded across all particle sizes investigated.

As a thermoplastic, PMMA softens and eventually melts with increasing temperature. In the molten state, particle-based dimensionless numbers are no longer applicable.

The thermal lag ΔT_1 was estimated according to Eq. (9) using the thermophysical properties of solid PMMA. Ideally, the properties of the PMMA melt should be employed. As these are not well stablished in the literature, the solid-state values were used as an approximation. The melt layer thickness δ_m was determined from the inner cross section area of the crucible, the material density and the initial sample mass ($\delta m = m_0/(\rho_m A_c)$, with $A_c = 2.827 \cdot 10^{-5}$m^2). As for the dimensionless numbers, the maximum heating rate was used to obtain a conservative upper-bound estimate. The resulting ΔT_1 values for the investigated sample masses (0.5–8 mg) range from 0.0024 to 0.0348 K (Table A.4) and are therefore negligible throughout.

The temperature deviation due to heat consumption during decomposition (ΔT_2) was estimated according to Eq. (10), using the same kinetic parameters (E_a, T_p) as for the Fourier number calculation and a shape parameter of $n = 2$ [27]. The calculated values range from 0.0078 K to 1.9965 K (Table A.4). Even the maximum value, obtained for the highest sample mass of 8 mg, remains small relative to the temperature range over which decomposition occurs and is therefore considered acceptable.

Taken together, neither the particle-scale nor the sample-scale analysis revealed evidence of significant heat transport limitations under the experimental conditions applied in this study, provided the assumed conditions hold.

3.2. Mass down-scaling

While the preceding theoretical assessment provides a useful first orientation, it relies on several simplifying assumptions and is limited to heat transfer processes, which may not necessarily reflect the real conditions within the sample. Furthermore, other transport limitations, such as mass transport, are not considered. An experimental verification was therefore conducted across different particle sizes and initial sample masses. The mass downscaling approach recommended by ICTAC [3] was applied in the present study to the powder 1, powder 8 and piece samples. The experiments were conducted at the maximum heating rate employed (30 K/min) and for initial sample masses in the range of 0.5–8 mg, see Fig. 2.

The dTG data were analysed, as curve congruence is most sensitively reflected in the first derivative. In particular, attention was focused on the main decomposition peak, which corresponds to the region of the highest conversion rate. In this region, any deviations caused by transport phenomena at different sample masses are particularly pronounced, making them easier to identify.

Overall, the results show that for all sample forms, increasing mass leads to a shift of the dTG curve towards higher temperatures. This effect is particularly evident for the piece samples, where congruent profiles of the main decomposition peak are observed only for masses of 1 mg or less.

The peak shape also provides evidence of a systematic distortion. Increasing mass consistently leads to broader peaks and, in some cases, to a slight asymmetry. This broadening occurs even in instances where the position of the main decomposition peak remains largely unchanged, indicating that mass-induced effects do not necessarily manifest as a peak shift, see for example the 2 mg powder 1 and powder 8 cases.

Deviations in the low-temperature region of the dTG profile (Fig. A.6) are exclusive to piece samples and only manifest at initial sample masses exceeding 2 mg, rendering them considerably less pronounced than the discrepancies observed at the main decomposition peak.

Taking into account the results of the theoretical analysis of heat transfer limitations Section 3.1, which indicate that neither the particle sizes nor the sample masses investigated here should lead to significant temperature shifts, the mass down-scaling results clearly demonstrate that relevant transport processes are nevertheless present when the initial sample mass is too high — suggesting either that a different mechanism than heat transfer limitation is responsible, or that the assumptions underlying the theoretical analysis were not appropriate for the conditions investigated here. Based on the results, a nominal mass of 1 mg was chosen for all sample forms in the subsequent investigations. Although higher nominal masses could theoretically have been used for the powder samples, the smallest common mass was selected to ensure uniform experimental conditions across all sample forms.

3.3. General decomposition behaviour

PMMA is known to decompose in multiple steps [21–23]. This is also the case in the present study, as shown in Fig. 3. However, the various sample forms exhibit markedly different decomposition patterns. Illustrated are the two representative forms at the extremes of particle size, namely the finest powder (powder 1) and the piece samples.

All sample forms exhibit a main decomposition peak, which, for $\beta = 30$ K min^{-1}, appears between approximately 350 and 450 °C. A pronounced shoulder appears immediately preceding the main peak, although the onset of decomposition differs markedly between the sample forms.

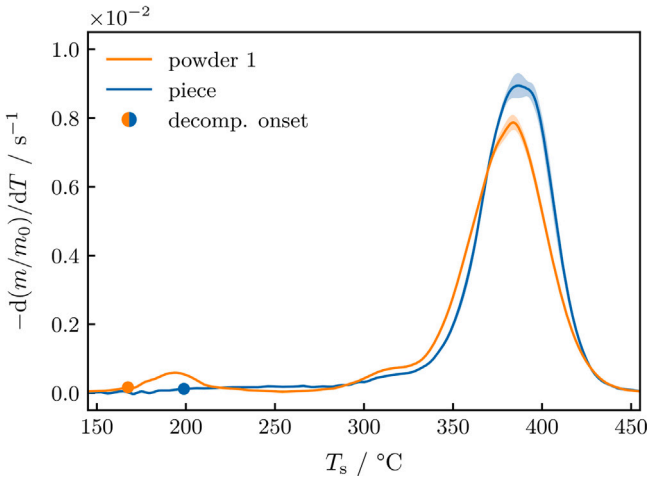

Fig. 3. dTG curves of powder 1 and piece at β = 30 K min^{-1} (m_0 = 1 mg; solid lines: average; shaded areas: standard deviation). Points mark the onset of decomposition (threshold: mass loss of at least 0.5%).

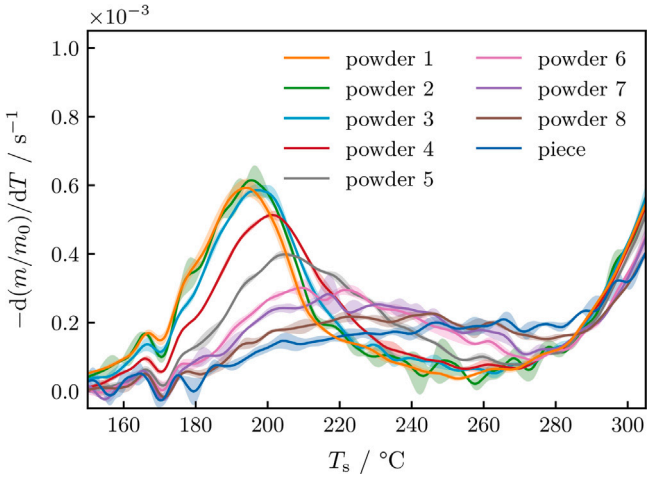

Fig. 4. Decomposition onset of the different sample forms at β = 30 K min^{-1} (m_0 = 1 mg; solid lines: average; shaded areas: standard deviation).

To enable a quantitative comparison between the two sample forms, the onset of decomposition was defined as the point at which 0.5% of the initial mass had been converted. According to this criterion, decomposition initiates at 167 °C for powder 1, whereas the corresponding onset for the piece sample occurs at 199 °C. The character of the early decomposition also differs: powder 1 exhibits a distinct, isolated low-temperature peak, while the piece sample shows a more gradual initial mass-loss behaviour.

Given that the initial stage of decomposition exhibits pronounced differences in decomposition characteristics between the sample forms, this phase was examined in greater detail. A closer analysis reveals a systematic trend with particle size, see Fig. 4. With increasing particle size, the decomposition behaviour transitions from a distinct, isolated early peak to a progressively more gradual mass-loss profile.

In addition, the shoulder and the main decomposition peak of the smallest and largest particle sizes appear to differ only marginally. However, the slight shift in peak position must be noted in any case. For Powder 1, both the shoulder and the peak occur somewhat earlier than in the case of the piece sample, while the shape of the main decomposition peak is broader for the piece.

3.4. Molecular weight distribution

To exclude molecular differences between the various sample forms – which are known to influence thermal decomposition behaviour [21] – GPC was carried out. Fig. 5 presents the molar-mass distributions of all samples, indicating that the PMMA under investigation is characterised by a comparatively high molar mass.

The molar mass distributions of the different sample forms show no significant differences. The minor variations observed in the low-molar-mass region are attributed to experimental variability. Likewise, neither the apparent number-average molar mass nor the apparent weight-average molar mass indicates a correlation between molar-mass distribution and particle size, see Table A.5. The broad distribution evident in the molar-mass profiles is reflected in the elevated dispersity values.

3.5. Evolved gas analysis

Evolved gas analysis (EGA) can provide further insight into the decomposition processes. FTIR analysis was therefore performed to investigate whether different reactions at low temperatures could explain the observed differences between the sample forms.

In general, thermal decomposition of PMMA primarily produces the monomer methyl methacrylate (MMA) via terminal and random bond scission [32]. This is reflected in the measured chemigram (evaluated wavenumber range 1261–1089 cm^{-1}), which closely matches the dTG signal and indicates that MMA is the dominant product throughout the entire decomposition range, including the low-temperature region (Fig. 6).

Apart from MMA, no other relevant components could be identified in the measured FTIR spectrum. Only trace amounts of carbon dioxide and background water vapour were detected. These showed no correlation with the dTG signal and were therefore not visualised here. In contrast, the low-temperature mass-loss peaks can be clearly associated with the release of MMA.

The EGA profiles reveal that mass loss is directly linked to the release of MMA, with the dTG signal showing good agreement with the MMA release profile. This behaviour is observed for all sample forms, indicating that no differing decomposition reactions occur. Consequently, the EGA results do not provide an explanation for the variations in decomposition behaviour between the sample forms and the FTIR analysis confirms that the nature of the decomposition products is consistent across all samples.

3.6. Temperature-dependent morphology

To assess whether morphological features provide indications for the observed differences between the various sample forms, the external structure of the samples was examined at defined temperature levels, see Fig. 7.

The investigated sample forms do not show significant morphological changes up to and including a temperature of 320 °C compared to their room-temperature state. Only powder 1 exhibits a light discolouration. More substantial changes occur within the main decomposition peak, where melting and bubble formation is observed in all cases.

If an intentionally excessive nominal mass (m_0 = 8 mg) is selected and investigated, the bubbles appear less clearly defined at 370 °C, see Fig. A.7.

3.7. Kinetic aspects

Given that micro-scale experimental data are intended to serve as the basis for kinetic modelling, it is essential to clarify how the results obtained for the different sample forms affect the kinetic description.

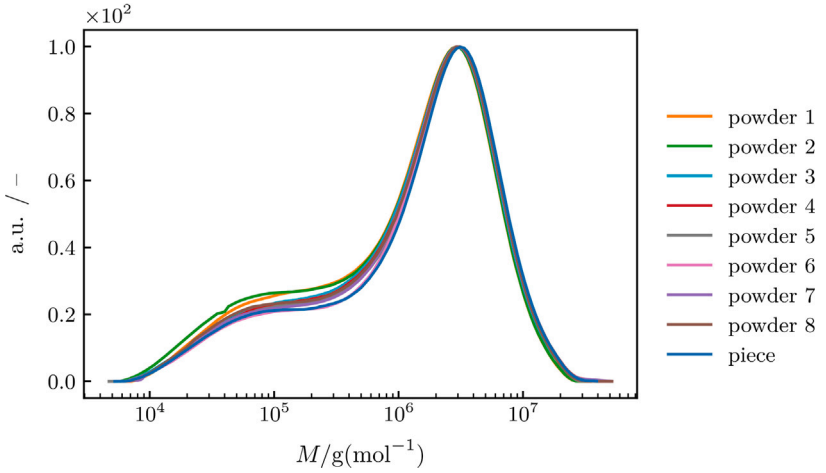

Fig. 5. Height-normalised (apparent) molar mass distribution of the various samples (a.u. denotes arbitrary unit).

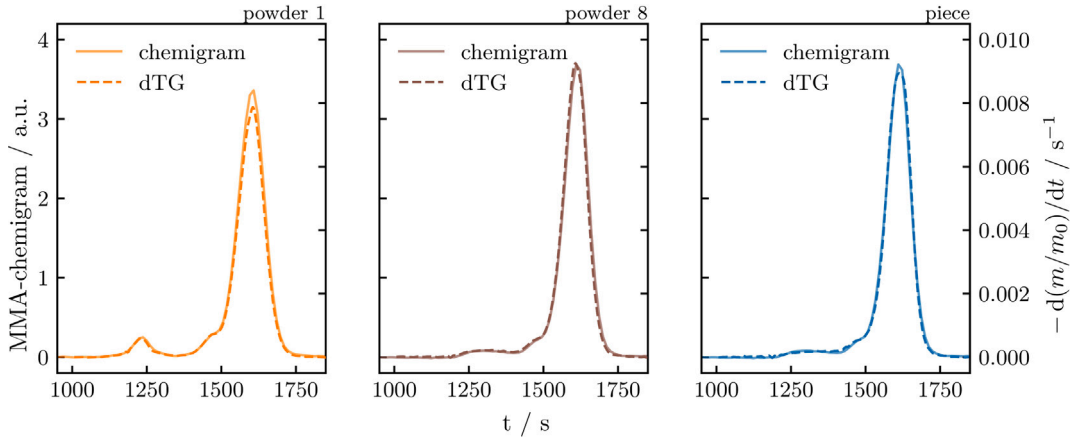

Fig. 6. Comparison of the chemigram for MMA (1261–1089 cm^{-1}) with the dTG signal of different sample forms at $\beta = 30$ K min^{-1} ($m_0 = 1$ mg).

As already indicated by the dTG profiles in Figs. 3 and 4, the thermal decomposition of PMMA proceeds via a multi-step process. With decreasing particle size, an increasingly pronounced contribution of decomposition reactions at lower temperatures is observed.

The multi-step character is also evident from the isoconversional analysis using the KAS method, see Fig. 8 and Table A.6. The resulting $E_{a,\alpha}$ values, plotted against the mass conversion α, indicate that the effective activation energies of the individual sample forms differ and that the mean activation energy systematically decreases with increasing particle size. In all cases, the deviations of the respective E_a values from the mean exceed 20%, which is a strong indication of a multi-step process [5].

However, the multiple decomposition steps appear to be independent of one another, as no heating-rate-dependent changes in the conversion profiles are observed, see Fig. A.8.

As indicated by the isothermal experimental data, the decomposition of PMMA can be well described by a decelerating reaction model [2], see Fig. A.9. For fine powder, low-temperature reactions lead to faster reaction rates at the onset of isothermal decomposition. From this behaviour it can be inferred that the effective kinetic descriptions differ between the investigated sample forms. While fine powder exhibits an almost immediate increase in conversion once the isothermal temperature is reached, coarser powder fractions and compact pieces show a delayed conversion onset and a systematically slower progression of the reaction.

The consequences of these sample-configuration-dependent kinetic parameters for fire spread modelling can be inferred from previous work [17]. Fig. 9 shows a fire spread scenario simulated with the Fire Dynamics Simulator (FDS) [33] in which the rate of flame spread across the black surface was examined, starting from an initial ignition area indicated in light grey in Fig. 9a. In both simulation cases – piece and powder – only the kinetic parameters required for pyrolysis modelling were varied, whilst all other model inputs remained identical. For full modelling details, the reader is referred to [17].

The PMMA investigated in the present work is the same material as used in the previous study, where a powder fraction of 75–250 µm was employed, corresponding to powders 2 to 5 of the current classification. The outcome of this simulation-based consequence analysis is unambiguous: the relatively minor differences in the STA data – from which the kinetic parameters were derived – translate into a substantially higher mean fire spread rate of approximately 0.36 cm/s for the powder case compared to 0.21 cm/s for the piece case, along with correspondingly distinct heat release rate profiles (Fig. 9b).

4. Discussion

The experimental results are interpreted in the following with respect to the central question posed in the introduction: what are the physical origins of the specimen-form-dependent decomposition behaviour observed for the black cast PMMA under investigation?

A first indication that mass transport processes may be responsible for the observed differences is provided by the systematic thermal analysis of the different sample forms, which revealed a direct correlation between particle size and the decomposition profile in the low-temperature region. At constant mass, the primary distinction between

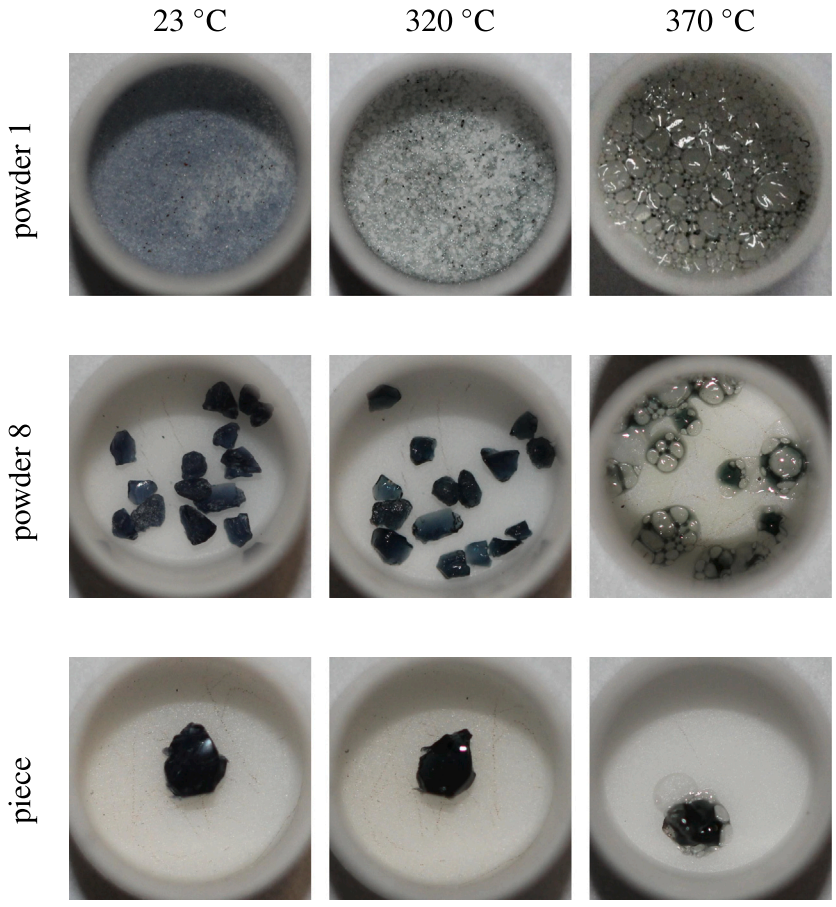

Fig. 7. External structure of powder 1, powder 8 and piece sample at 23, 320 and 370 °C (β = 30 K min^{-1}, m_0 = 1 mg).

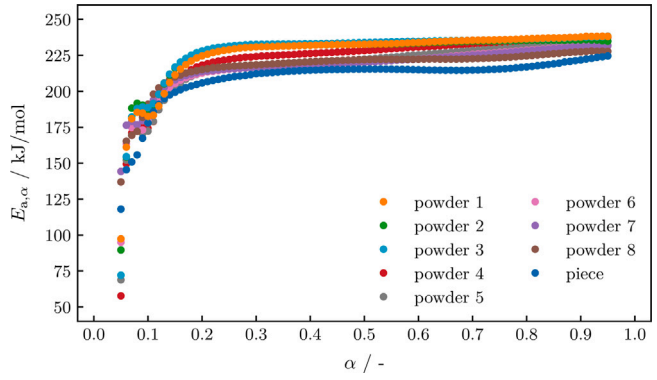

Fig. 8. Conversion dependent apparent activation energies ($E_{a,\alpha}$) for the different sample forms ($0.05 \leq \alpha \leq 0.95$).

the sample forms arises from the increasing surface-to-volume ratio with decreasing particle size: as particle size increases, the initially isolated mass-loss peak gradually evolves into a more continuous mass-loss profile without a clear peak shape. Before attributing this behaviour to mass transport, alternative explanations had to be considered and ruled out.

The possibility that differences in decomposition behaviour arise from variations in heating behaviour was addressed by the theoretical analysis of heat transfer limitations and the mass down-scaling experiments. The Biot and Fourier number analysis confirmed that intra-particle heat transfer limitations are negligible across all particle sizes investigated and the estimated temperature deviations due to thermal lag and endothermic decomposition were found to be small throughout the investigated mass range. In the mass down-scaling experiments, undistorted dTG results were only obtained at lower sample masses, which served as an indicator that – given heat transfer limitations had already been excluded through the theoretical analysis – other transport limitations may be present. Only at a nominal sample mass of 1 mg did systematic deviations appear to be absent. The evolved gas analysis demonstrated that the fundamental decomposition mechanism is consistent across all sample forms: all samples decomposed to the monomer MMA, as evidenced by the congruence of the dTG and chemigram profiles, providing no indication that differences in decomposition chemistry contribute to the observed behaviour. GPC measurements were conducted to assess whether the powder production process introduced material alterations through cryo-milling. No significant differences in molar mass distribution were found between the sample forms. The FTIR results corroborate this finding. Since the nature and composition of the decomposition products were consistent across all sample forms, no indication of material alterations is provided by the decomposition characteristics either. Whilst microstructural changes due to cryo-milling cannot be conclusively excluded, neither analysis provides any strong evidence that such alterations represent a primary driver of the observed behaviour. Taken together, these results consistently point away from heat transfer limitations, changes in decomposition chemistry and material alterations as primary drivers of the observed differences.

The morphological investigations provided direct support for the hypothesis that the observed differences are governed by mass transport. Prior to the main decomposition peak, the external structure of all sample forms remained largely unchanged relative to their initial state, indicating that no significant morphological transformation occurs in the low-temperature region. This observation suggests that, as particle

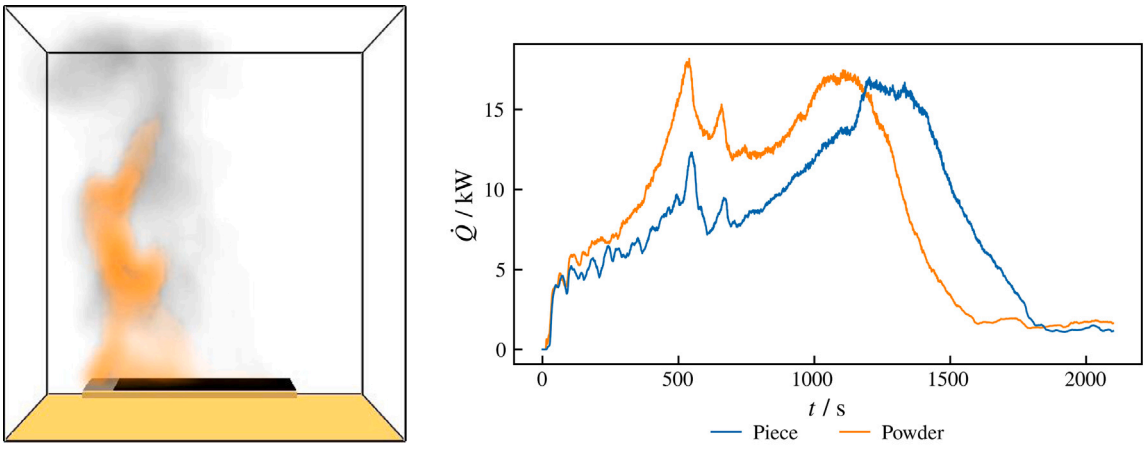

(a) Simulation setup (gray area is ignition area, black area is spread area).

(b) Heat release rate.

Fig. 9. Simulation results from [17] illustrating the influence of kinetic parameters derived from PMMA powder and piece specimens on fire spread predictions.

size increases, the diffusion path within the solid matrix becomes longer, delaying the onset of detectable mass loss, since mass loss is only measurable once the generated gas has escaped from the particle. The systematic transition from a distinct, isolated low-temperature peak in the finest powder to a progressively more gradual mass-loss profile with increasing particle size is consistent with this interpretation and supports a diffusion-limited gas release mechanism through the solid matrix as the dominant transport process in the low-temperature region.

During the main decomposition peak, the transport regime shifts fundamentally. Visible melting and bubble formation were observed across all sample forms, indicating that gas release is no longer governed by solid-state diffusion but by convective bubble transport through the polymer melt. The differences in the position and shape of the main decomposition peak between sample forms can be attributed to differences in the effective surface area available for gas escape. In the crucible, powder samples are more evenly distributed across the crucible bottom, providing a larger effective area than the compact piece sample. The high molar mass of the investigated PMMA, as confirmed by GPC, leads to the formation of a highly viscous melt, which impedes bubble mobility and renders the bubble transport properties sensitive to the overall sample mass. This is reflected in the morphological comparison between samples of different masses: at 1 mg, clearly defined bubble structures are observed, whereas at 8 mg the bubble structure seems less well-defined, indicating that a larger melt volume further restricts bubble transport. This mass-dependence provides a mechanistic explanation for the transport-induced deviations observed in the mass down-scaling experiments, deviations that were not anticipated by any of the preceding theoretical analyses, since these are inherently limited to thermal phenomena and do not account for mass transport effects. It should furthermore be noted that the validity of such theoretical approaches may be questioned even on the level of their underlying assumptions, as the thermophysical properties of a polymer melt are difficult to estimate reliably and the occurrence of decomposition accompanied by bubble formation gives rise to a physical situation that is inherently too complex to be captured by simple analytical estimates. This underlines that experimental verification via mass down-scaling is obligatory, as theoretical estimates alone are insufficient to identify the full range of transport limitations present in a given material. Moreover, the morphological observations demonstrate that a true 0D-condition cannot be achieved for the PMMA under investigation, as bubble formation and the associated gas transport within the melt persist even at the sample masses identified as adequate in the mass down-scaling, though the resulting delays can be minimised by selecting a sufficiently low sample mass.

The experimental results thus consistently point to two distinct, specimen-form-dependent transport regimes: diffusion-limited gas release through the solid matrix in the low-temperature region and convective bubble transport through the polymer melt during the main decomposition peak. Both regimes have direct consequences for the kinetic description derived from micro-scale experiments. The isoconversional analysis showed that the apparent activation energies differ systematically between sample forms and decrease with increasing particle size, whilst the isothermal experiments confirmed that the effective kinetic descriptions differ between sample forms in terms of both the onset and the progression of conversion. These differences are not an artefact of the experimental procedure but reflect the transport regime captured by the respective specimen form: fine powders are governed by short diffusion paths and a large effective surface area, whilst coarser fractions and piece samples are increasingly influenced by longer diffusion paths and, during the main peak, by the rheological properties of the melt. Since any kinetic description derived from micro-scale experiments will inevitably reflect the transport regime of the chosen specimen form, the choice of specimen form directly determines which transport processes are encoded in the kinetic parameters and, as demonstrated by the fire spread simulations in previous work, this choice ultimately affects the predicted rate of fire spread. Whilst the present results clarify the physical origin of these specimen-form-dependent differences, they do not resolve the broader question of which specimen form constitutes a representative test specimen in the context of fire science — a question that, as noted in the introduction, remains without a clear and unambiguous answer given the wide range of specimen geometries commonly employed in the field.

5. Conclusion and outlook

Through a comprehensive experimental investigation, it was established that the specimen-form-dependent differences in decomposition behaviour observed for the black cast PMMA under investigation are most likely attributable to mass transport restrictions. In the low-temperature region, the dominant transport mechanism is diffusion-limited gas release through the solid matrix, whilst during the main decomposition peak the transport regime shifts to convective bubble transport. The kinetic analysis demonstrated that the derived kinetic parameters are implicitly influenced by these processes. The choice of specimen form is therefore not a procedural detail, but a critical factor in the derivation of kinetic parameters, with direct consequences for fire spread predictions. These findings underline that, wherever specimen-form-dependent differences in decomposition behaviour are observed, their underlying causes must be identified before a specimen

form can be selected with confidence — since only a form whose transport processes reflect those of the material in the application scenario of interest will yield representative kinetic parameters.

For the present material, this selection cannot yet be made with certainty. The original objective of ensuring compliance with the 0D-assumption proved difficult to achieve: despite the implementation of established experimental standards, specifically the ICTAC recommendations, transport-free decomposition could not be attained. Notably, without the extended investigations carried out beyond these standard guidelines, the influence of gas transport limitations would likely have gone undetected. Mass down-scaling alone, for instance, would have suggested that no transport limitations are present at a nominal sample mass of 1 mg — a conclusion that, as demonstrated in this study, does not hold.

The question of which specimen form yields the most representative kinetic parameters for use in fire modelling can therefore only be resolved through validation against real-scale experimental data, which should constitute the next step. More broadly, it may also be necessary to reconsider whether the strict requirement of achieving 0D-conditions is meaningful in this context, given that fire models inherently rely on simplifications and approximations and therefore require effective rather than intrinsic material properties [34].

Whilst the present investigation was focused on black cast PMMA, the complementary measurements conducted on additional materials demonstrated that specimen-form-dependent decomposition behaviour is not confined to a single material but is rather material-dependent in its occurrence. Whilst the underlying causes may differ across materials, the results collectively highlight that a systematic assessment of specimen-form effects should be considered a standard component of any experimental programme aimed at deriving kinetic parameters for pyrolysis modelling. Given the potential consequences for kinetic parameter reliability and fire spread prediction accuracy, such assessments are of broad relevance to the fire science community.

CRediT authorship contribution statement

Felix Armbrust: Writing – review & editing, Writing – original draft, Visualization, Validation, Resources, Project administration, Methodology, Investigation, Formal analysis, Data curation, Conceptualization. **Tristan Hehnen:** Writing – review & editing, Conceptualization. **Jochen Zehfuß:** Writing – review & editing, Supervision, Funding acquisition, Resources. **Olaf Riese:** Writing – review & editing. **Lukas Arnold:** Writing – review & editing, Funding acquisition.

Declaration of competing interest

The authors declare that they have no known competing financial interests or personal relationships that could have appeared to influence the work reported in this paper.

Acknowledgements

The authors are grateful for the funding of the Fire Research Center (ZeBra) by the Deutsche Forschungsgemeinschaft and the State of Lower Saxony, without the experimental investigations would not have been possible.

This work was partly supported by the German Federal Ministry of Education and Research through the BESKID project (grant numbers 13N16390 and 13N16392), and by the German Federal Ministry for the Environment, Climate Action, Nature Conservation and Nuclear Safety (grant number 1501696).

Appendix

See Figs. A.1–A.9 and Tables A.1–A.6.

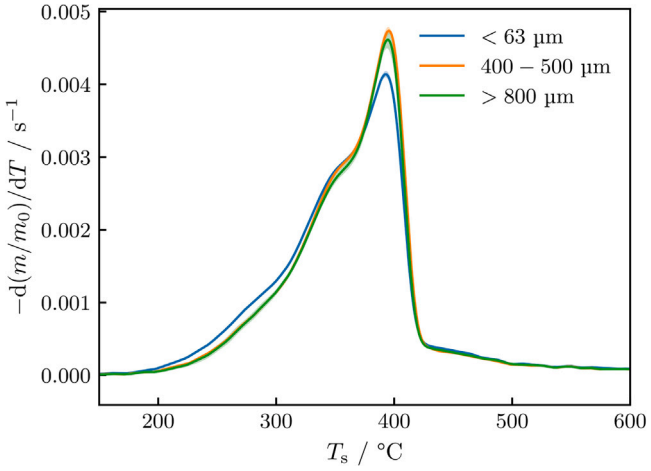

Fig. A.1. dTG results for different particle sizes of pine wood, investigated in the context of the MaCFP-4 project [35], showing specimen-form-dependent deviations in the early stage of decomposition. The adequacy of the sample mass was verified by means of mass down-scaling (β = 30 K min^{-1}, m_0 = 1 mg; solid lines represent the average of three replicates; shaded areas: standard deviation).

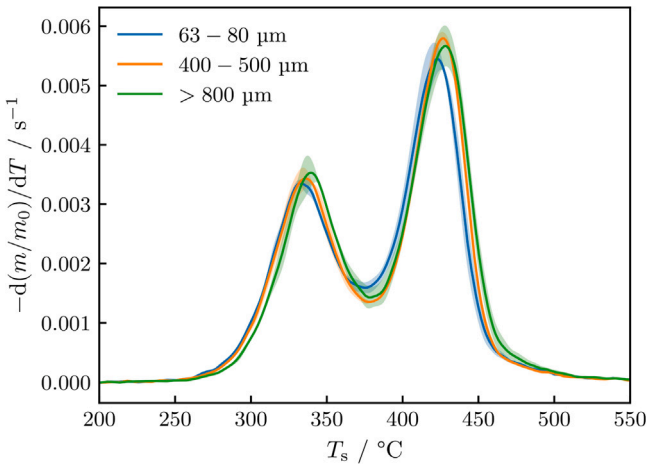

Fig. A.2. dTG results for different particle sizes of polyurethane, showing specimen-form-dependent shifts to higher temperatures. The adequacy of the sample mass was verified by means of mass down-scaling (β = 30 K min^{-1}, m_0 = 1 mg; solid lines represent the average of three replicates; shaded areas: standard deviation).

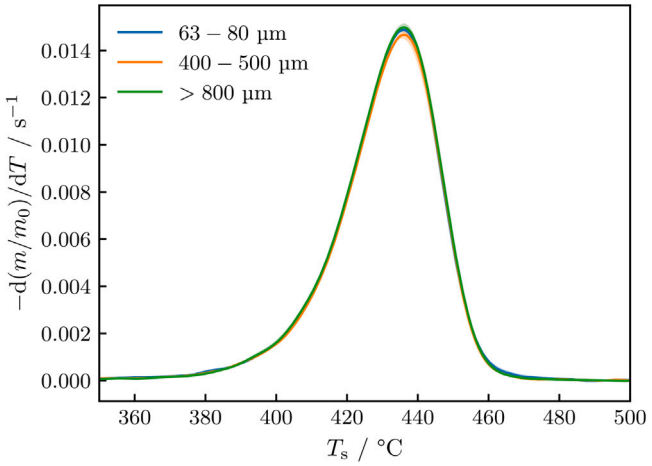

Fig. A.3. dTG results for different particle sizes of polystyrene with no influence of the specimen form. The adequacy of the sample mass was verified by means of mass down-scaling (β = 30 K min^{-1}, m_0 = 1 mg; solid lines represent the average of three replicates; shaded areas: standard deviation).

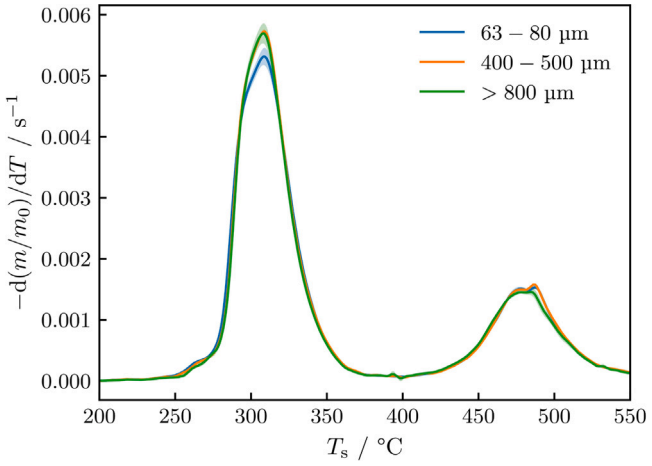

Fig. A.4. dTG results for different particle sizes of polyvinylchloride with no influence of the specimen form. The adequacy of the sample mass was verified by means of mass down-scaling (β = 30 K min^{-1}, m_0 = 1 mg; solid lines represent the average of three replicates; shaded areas: standard deviation).

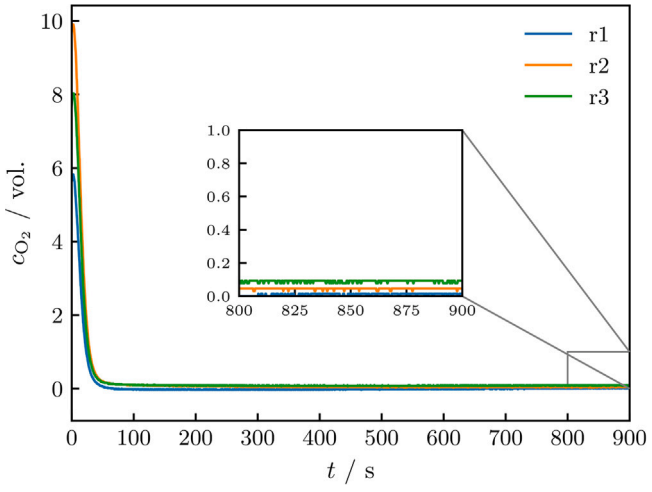

Fig. A.5. Oxygen concentration measurement (c_{O_2}) during the 15-minute pre-purge phase to verify the establishment of a quasi-inert atmosphere.

Table A.1
Parameters for the calculation of Bi, Fo, ΔT_1 and ΔT_2.

Parameter	Value
$\lambda = \lambda_m$	0.19 Wm^{-1}K^{-1} [36]
$\rho = \rho_m$	1190 kg m^{-3} [36]
$c_p = c_{p,m}$	1470 J(kg K)$^{-1}$ [36]
λ_{Fluid}	0.044 Wm^{-1}K^{-1} [37]
ρ_{Fluid}	0.5160 kg m^{-3} [37]
μ	$3.09 \cdot 10^{-5}$ Pa s [37]
$c_{p,fluid}$	1044 J(kg K)$^{-1}$ [37]
λ_c	30 Wm^{-1}K^{-1} [27]
ρ_c	3800 kg m^{-3} [27]
$c_{p,c}$	800 J(kg K)$^{-1}$ [27]
δ_c	0.6 mm [27]
Δh_g	1,600 kJ kg^{-1} [38]
R	8.31446 J mol^{-1}K^{-1}

Table A.2
Biot numbers for different samples and the case of conductive and convective heat transfer (case (ii)).

Sample	Bi for case 2 (-)
Powder 1	0.079
Powder 2	0.079
Powder 3	0.079
Powder 4	0.080
Powder 5	0.083
Powder 6	0.081
Powder 7	0.081
Powder 8	0.083
Piece	0.083

Table A.3
Fourier numbers for different samples.

Sample	Fo (-)
Powder 1	34,944
Powder 2	27,129
Powder 3	15,049
Powder 4	5699
Powder 5	2219
Powder 6	1132
Powder 7	685
Powder 8	247
Piece	139

Table A.4
Estimated temperature deviation based on empirical approaches.

Initial sample mass (mg)	ΔT_1 (K)	ΔT_2 (K)
0.5	0.0024	0.0078
1.0	0.0028	0.0312
2.0	0.0043	0.1248
4.0	0.0104	0.4991
8.0	0.0348	1.9965

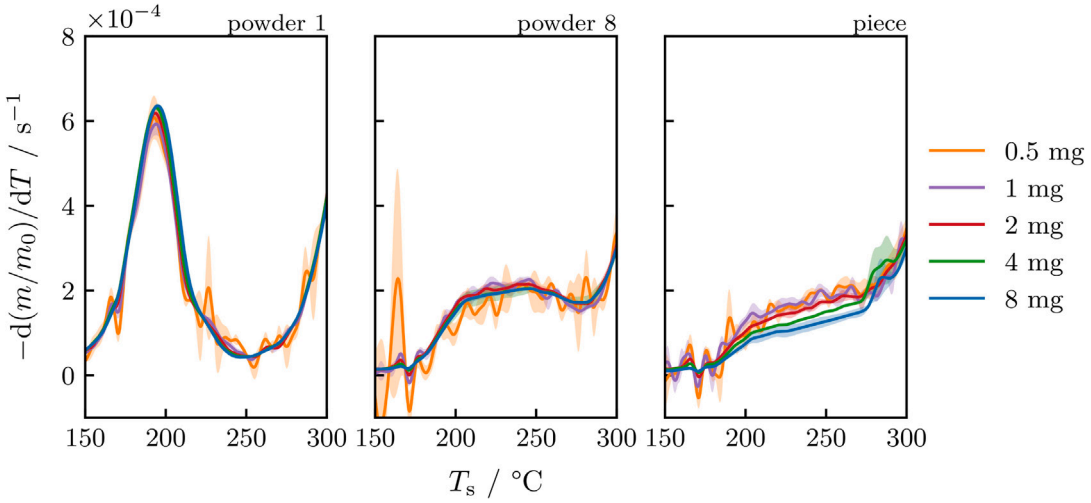

Fig. A.6. dTG signal comparison for the mass down-scaling. Focus on low-temperature range of the decomposition of powder 1, powder 8 and the piece sample at $\beta = 30$ K min^{-1} (solid lines: average; shaded areas: standard deviation).

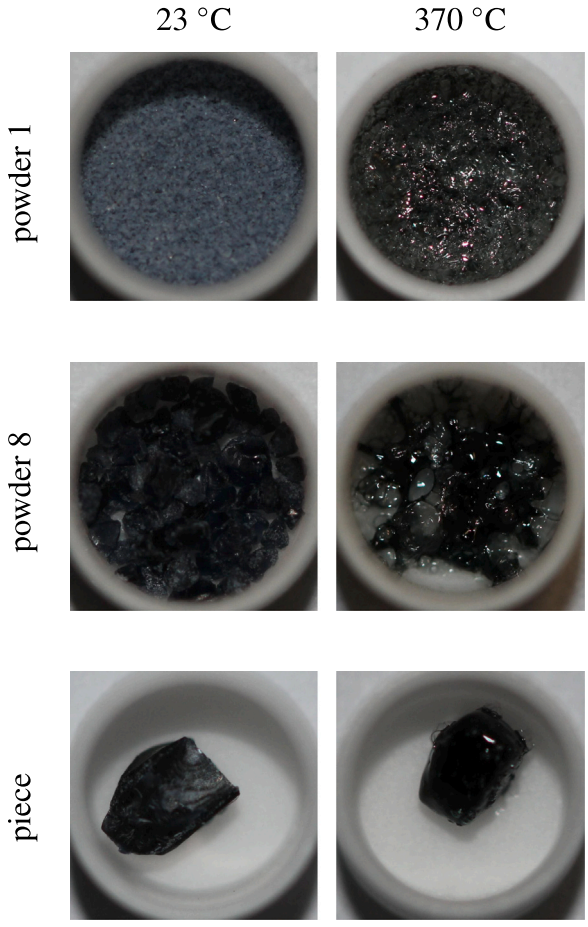

Fig. A.7. External structure of powder 1, powder 8 and piece sample at 23 and 370 °C for a high nominal mass ($\beta = 30$ K min^{-1}, $m_0 = 8$ mg).

Table A.5
Apparent number-average molar mass, weight-average molar mass and dispersity of the samples.

Sample	M_n^* (g mol^{-1})	M_w^* (g mol^{-1})	Đ (-)
Probe	M_n^* (g mol^{-1})	M_w^* (g mol^{-1})	Đ
Powder 1	213,000	2,560,000	12.0
Powder 2	183,000	2,530,000	13.9
Powder 3	218,000	2,740,000	12.6
Powder 4	225,000	2,890,000	12.9
Powder 5	227,000	2,860,000	12.6
Powder 6	234,000	2,910,000	12.4
Powder 7	227,000	2,850,000	12.6
Powder 8	217,000	2,170,000	12.8
Piece	230,000	2,300,000	12.9

Table A.6
Mean apparent activation energy ($E_{a,mean}$) and relative range for each sample type.

Sample	$E_{a,mean}$ (kJ mol^{-1})	Relative range (%)
Powder 1	226.62	62.20
Powder 2	226.88	64.50
Powder 3	227.68	73.05
Powder 4	221.85	81.09
Powder 5	217.52	76.42
Powder 6	216.69	63.34
Powder 7	217.72	40.18
Powder 8	217.38	41.92
Piece	209.48	50.89

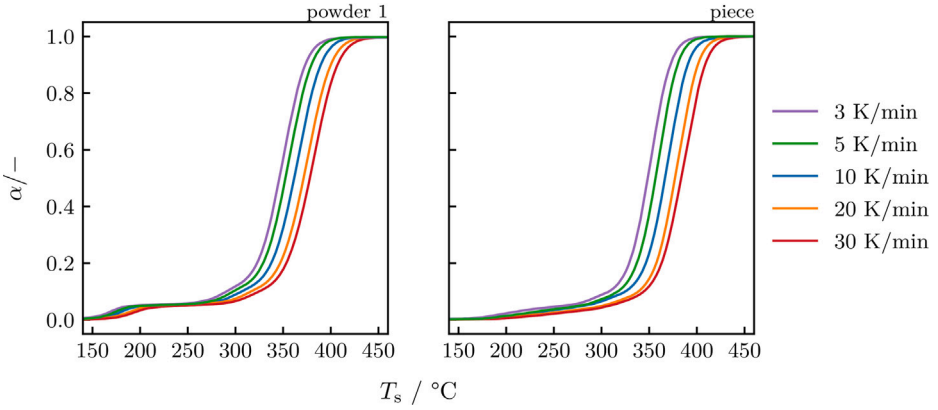

Fig. A.8. Heating-rate dependent course of the conversion for powder - and piece samples (solid lines: average).

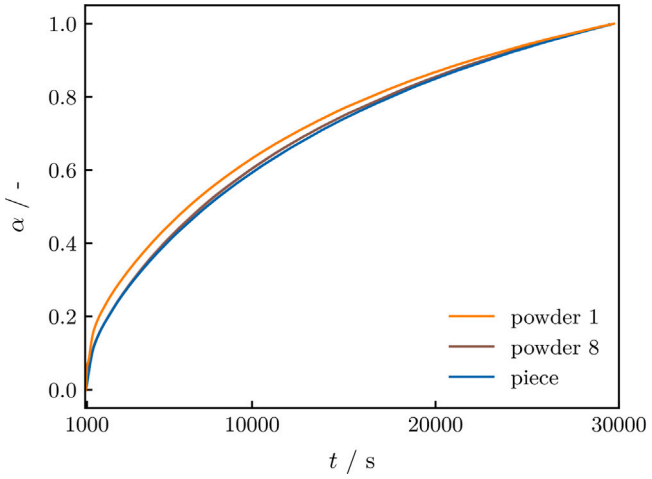

Fig. A.9. Isothermal conversion profiles of powder 1, powder 8 and the piece sample at an isothermal temperature of 300 °C (m_0 = 1 mg). Heating to the target isothermal temperature is performed after the initial settling phase (up to t = 900 s).

Data availability

Part of the experimental data is publicly available in the institutional repository of the Technische Universität Braunschweig at https://doi.org/10.24355/dbbs.084-202606100939-0.

References

[1] S.I. Stoliarov, Y. Ding, Pyrolysis model parameterization and fire growth prediction: The state of the art, Fire Saf. J. (2023) http://dx.doi.org/10.1016/j.firesaf.2023.103905.

[2] S. Vyazovkin, A.K. Burnham, J.M. Criado, L.A. Pérez-Maqueda, C. Popescu, N. Sbirrazzuoli, ICTAC kinetics committee recommendations for performing kinetic computations on thermal analysis data, Thermochim. Acta 520 (2011) http://dx.doi.org/10.1016/j.tca.2011.03.034.

[3] S. Vyazovkin, K. Chrissafis, M.L. Di Lorenzo, N. Koga, M. Pijolat, B. Roduit, N. Sbirrazzuoli, J.J. Suñol, ICTAC kinetics committee recommendations for collecting experimental thermal analysis data for kinetic computations, Thermochim. Acta 590 (2014) http://dx.doi.org/10.1016/j.tca.2014.05.036.

[4] S. Vyazovkin, Computational aspects of kinetic analysis, Thermochim. Acta (2000) http://dx.doi.org/10.1016/s0040-6031(00)00445-7.

[5] S. Vyazovkin, A.K. Burnham, L. Favergeon, N. Koga, E. Moukhina, L.A. Pérez-Maqueda, N. Sbirrazzuoli, ICTAC kinetics committee recommendations for analysis of multi-step kinetics, Thermochim. Acta (2020) http://dx.doi.org/10.1016/j.tca.2020.178597.

[6] International Organization for Standardization, Plastics – thermogravimetry (tg) of polymers (iso 11358-1:2022), Standard, ISO, Geneva, 2022.

[7] International Organization for Standardization, Plastics – differential scanning calorimetry (dsc) (iso 11357-1:2023), Standard, ISO, Geneva, 2023.

[8] ASTM International, Standard test method for determining flammability characteristics of plastics and other solid materials using microscale combustion calorimetry (astm d7309-21b), Standard, ASTM International, West Conshohocken, 2021.

[9] S.I. Stoliarov, S. Crowley, R.N. Walters, R.E. Lyon, Prediction of the burning rates of charring polymers, Combust. Flame (2010) http://dx.doi.org/10.1016/j.combustflame.2010.03.011.

[10] T. Fateh, T. Rogaume, J. Luche, F. Richard, F. Jabouille, Kinetic and mechanism of the thermal degradation of a plywood by using thermogravimetry and Fourier-transformed infrared spectroscopy analysis in nitrogen and air atmosphere, Fire Saf. J. (2013) http://dx.doi.org/10.1016/j.firesaf.2013.01.019.

[11] D. Bakirtzis, A. Ramani, J. Zhang, M.A. Delichatsios, Simplified structure of the condensed phase of fire retarded PA6 nanocomposites in TGA as related flammability, Fire Saf. J. (2014) http://dx.doi.org/10.1016/j.firesaf.2014.08.006.

[12] P.M. Doley, A.C.Y. Yuen, I. Kabir, L. Liu, C. Wang, T.B.Y. Chen, G.H. Yeoh, Thermal hazard and smoke toxicity assessment of building polymers incorporating TGA and FTIR—Integrated cone calorimeter arrangement, Fire (2022) http://dx.doi.org/10.3390/fire5050139.

[13] O.Y. Fetisova, N.M. Mikova, A.I. Chudina, A.S. Kazachenko, Kinetic study of pyrolysis of coniferous bark wood and modified fir bark wood, Fire (2023) http://dx.doi.org/10.3390/fire6020059.

[14] K. De Lannoye, C. Trettin, A. Belt, E. Reinecke, R. Goertz, L. Arnold, The influence of experimental conditions on the mass loss for TGA in fire safety science, Fire Saf. J. (2024) http://dx.doi.org/10.1016/j.firesaf.2023.104079.

[15] Y. Gao, S. Feng, L. Yan, T. Chu, Z. Wang, J. Xiao, H. Xie, J. Zhang, Z. Wang, Flame retardancy of densified wood modified by bio-material based flame retardant, Fire Technol. (2024) http://dx.doi.org/10.1007/s10694-024-01594-w.

[16] M. Brown, Introduction to Thermal Analysis, Kluwer Academic Publishers, 2004, http://dx.doi.org/10.1007/0-306-48404-8.

[17] F. Armbrust, T. Hehnen, J. Zehfuß, O. Riese, L. Arnold, Influence of experiemntal boundary conditions on kinetic models for fire spread predictions, in: J. Zehfuß (Ed.), Proceedings of the 11th Symposium Structural Fire Enginnering - TU Braunschweig 2025, Braunschweig, Germany, 2025, http://dx.doi.org/10.24355/dbbs.084-202601131025-0.

[18] T.L.S. Quaresma, T. Hehnen, L. Arnold, The influence of small mass loss rate peaks on the rate of spread of predictive flame spread simulations: A theoretical study, Fire Saf. J. (2025) http://dx.doi.org/10.1016/j.firesaf.2025.104344.

[19] M.J. DiDomizio, M. McKinnon, Impact of specimen preparation method on thermal analysis testing and derived parameters, in: Obtaining Data for Fire Growth Models, ASTM International, 2023, http://dx.doi.org/10.1520/stp164220210106.

[20] H.R. Oswald, H.G. Wiedemann, Factors influencing thermoanalytical curves, J. Therm. Anal. (1977) http://dx.doi.org/10.1007/bf01909472.

[21] M. Ferriol, A. Gentilhomme, M. Cochez, N. Oget, J.L. Mieloszynski, Thermal degradation of poly(methyl methacrylate) (PMMA): modelling of DTG and TG curves, Polym. Degrad. Stab. (2003) http://dx.doi.org/10.1016/s0141-3910(02)00291-4.

[22] T. Hirata, T. Kashiwagi, J.E. Brown, Thermal and oxidative degradation of poly(methyl methacrylate): weight loss, Macromolecules (1985) http://dx.doi.org/10.1021/ma00149a010.

[23] B.J. Holland, J.N. Hay, The effect of polymerisation conditions on the kinetics and mechanisms of thermal degradation of PMMA, Polym. Degrad. Stab. (2002) http://dx.doi.org/10.1016/s0141-3910(02)00100-3.

[24] M. Brown (Ed.), Principles and practice, in: Handbook of Thermal Analysis and Calorimetry, vol. 1, Elsevier Science BV, Amsterdam, ISBN: 978-0-444-82085-3, 1998.

[25] W.E. Ranz, W.R. Marshall, Evaporation from drops, Chem. Eng. Prog. 48 (1952).

[26] R.E. Lyon, R.N. Walters, S.I. Stoliarov, N. Safronava, Principles and practice of microscale combustion calorimetry, Tech. rep. DOT/FAA/TC-12/53(R1), (DOT/FAA/TC-12/53(R1)) Federal Aviation Administration, William J. Hughes Technical Center, Aviation Research Division, Atlantic City International Airport, New Jersey, 2013.

[27] A.Y. Snegirev, M.K. Handawy, V.V. Stepanov, V.A. Talalov, Pyrolysis and combustion of polymer mixtures: Exploring additivity of the heat release rate, Polym. Degrad. Stab. 161 (2019) http://dx.doi.org/10.1016/j.polymdegradstab.2019.01.037.

[28] R.E. Lyon, N. Safronava, J. Senese, S.I. Stoliarov, Thermokinetic model of sample response in nonisothermal analysis, Thermochim. Acta (2012) http://dx.doi.org/10.1016/j.tca.2012.06.034.

[29] Organisation for Economic Co-operation and Development, OECD Guideline for the Testing of Chemicals No. 118: Determination of the Number-Average Molecular Weight and the Molecular Weight Distribution of Polymers using Gel Permeation Chromatography, Tech. rep., OECD, Paris, 1996.

[30] T. Hehnen, FireSciPy: Fundamental algorithms from the field of fire science, for computations with python, 2025, https://github.com/FireDynamics/FireSciPy.

[31] M.J. Starink, The determination of activation energy from linear heating rate experiments: a comparison of the accuracy of isoconversion methods, Thermochim. Acta (2003) http://dx.doi.org/10.1016/S0040-6031(03)00144-8.

[32] W.R. Zeng, S.F. Li, W.K. Chow, Review on chemical reactions of burning poly(methyl methacrylate) PMMA, J. Fire Sci. (2002) http://dx.doi.org/10.1177/0734904102020005482.

[33] Kevin McGrattan, et al., Fire Dynamics Simulator (FDS), 2025, https://github.com/firemodels/fds/releases, Version FDS-6.9.1-0-g889da6a-release.

[34] M. Faghri, B. Sunden (Eds.), Transport phenomena in fires, in: Developments in Heat Transfer, WIT Press, Southampton, England, 2008.

[35] International Association for Fire Safety Science , https://iafss.org/macfp/, Measurement & Computation of Fire Phenomena (MaCFP Working Group).

[36] POLYVANTIS GmbH, PLEXIGLAS GS/XT: Technical Information – Solid Sheet, Block, Multi-Skin Sheet, Corrugated Sheet, Tube and Rod, Tech. rep. Ref. No. 211-1, 2025, (Accessed 23 April 2026). POLYVANTIS GmbH URL https://www.plexiglas.de/files/plexiglas-content/pdf/technische-informationen/211-1-EN-PLEXIGLAS-GS-XT.pdf.

[37] E.W. Lemmon, R.T. Jacobsen, Viscosity and thermal conductivity equations for nitrogen, oxygen, argon, and air, Int. J. Thermophys. (2004) http://dx.doi.org/10.1023/b:ijot.0000022327.04529.f3.

[38] M.J. (chief editor) Hurley (Ed.), SFPE Handbook of Fire Protection Engineering, Springer New York, 2016, http://dx.doi.org/10.1007/978-1-4939-2565-0.

Update

Fire Safety Journal
Volume 165, Issue , November 2026, Page

DOI: https://doi.org/10.1016/j.firesaf.2026.104939

Fire Safety Journal 165 (2026) 104939

Contents lists available at ScienceDirect

Fire Safety Journal

journal homepage: www.elsevier.com/locate/firesaf

Corrigendum to "Sample-form-induced transport effects in the micro-scale decomposition of PMMA" [Fire Saf. J. 164 (2026) 104897]

Felix Armbrust [a,*], Tristan Hehnen [b], Jochen Zehfuß [a], Olaf Riese [a], Lukas Arnold [b,c]

[a] Institute of Building Materials, Concrete Construction and Fire Safety, Fire Research Center, Technische Universität Braunschweig, Beethovenstraße 52, Braunschweig, 38106, Germany
[b] Chair of Computational Civil Engineering, University of Wuppertal, Pauluskirchstraße 7, Wuppertal, 42285, Germany
[c] Institute of Advanced Simulation, Forschungszenrum Jülich, Wilhelm-Johnen-Straße, Jülich, 52428, Germany

The authors regret that minor typographical errors were present in the axis labels of certain figures in the published article. These typographical errors do not affect the content, interpretation, or conclusions of the paper. However, they are hereby corrected in this Corrigendum. The authors apologise for any inconvenience these errors may have caused.

In Figs. 2–4, A.1-A.4, and A.6, dT should be replaced by dt in the y-axis label, where t denotes time.

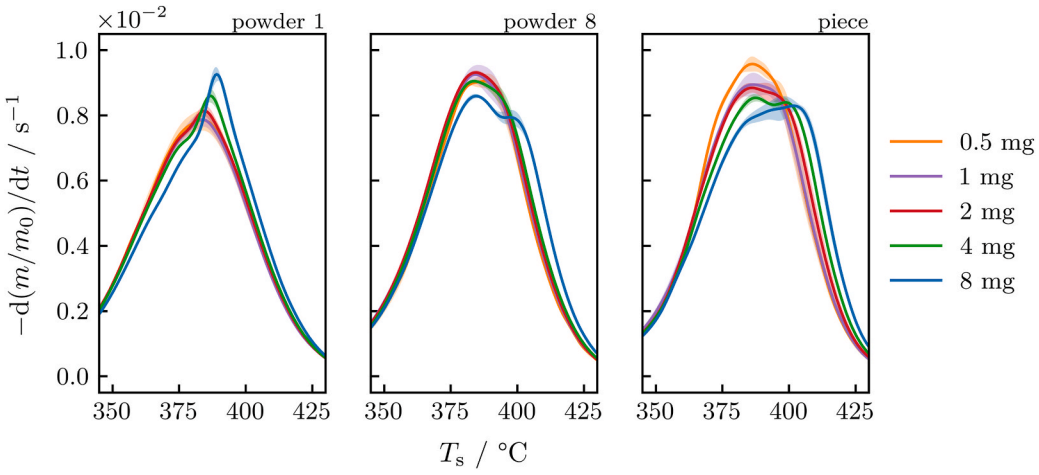

Fig. 2. dTG signal comparison for the mass down-scaling. Focus is on the main decomposition peak of powder 1, powder 8 and the piece sample at $\beta = 30$ K min^{-1} (solid lines: average; shaded areas: standard deviation).

DOI of original article: https://doi.org/10.1016/j.firesaf.2026.104897.
* Corresponding author.
E-mail address: felix.armbrust1@tu-braunschweig.de (F. Armbrust).

https://doi.org/10.1016/j.firesaf.2026.104939

Available online 31 July 2026
0379-7112/© 2026 The Author(s). Published by Elsevier Ltd. This is an open access article under the CC BY license (http://creativecommons.org/licenses/by/4.0/).

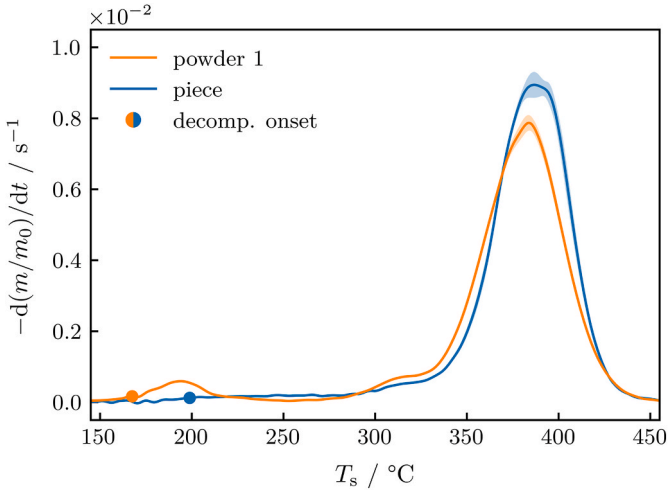

Fig. 3. dTG curves of powder 1 and piece at $\beta = 30\,\mathrm{K\ min^{-1}}$ ($m_0 = 1$ mg; solid lines: average; shaded areas: standard deviation). Points mark the onset of decomposition (threshold: mass loss of at least 0.5 %).

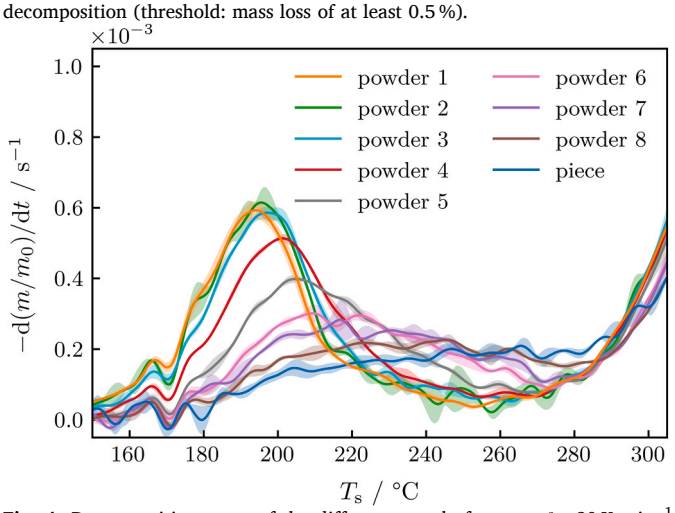

Fig. 4. Decomposition onset of the different sample forms at $\beta = 30\,\mathrm{K\ min^{-1}}$ ($m_0 = 1$ mg; solid lines: average; shaded areas: standard deviation).

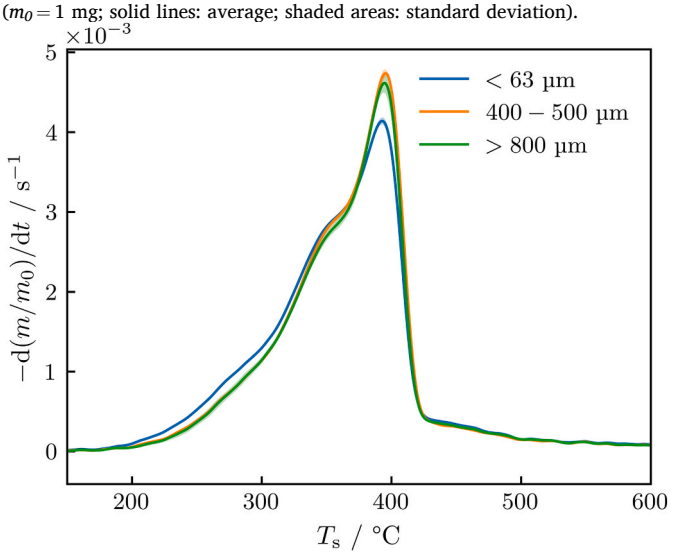

Fig. A.1. dTG results for different particle sizes of pine wood, investigated in the context of the MaCFP-4 project [35], showing specimen-form-dependent deviations in the early stage of decomposition. The adequacy of the sample mass was verified by means of mass down-scaling ($\beta = 30\,\mathrm{K\ min^{-1}}$, $m_0 = 1$ mg; solid lines represent the average of three replicates; shaded areas: standard deviation).

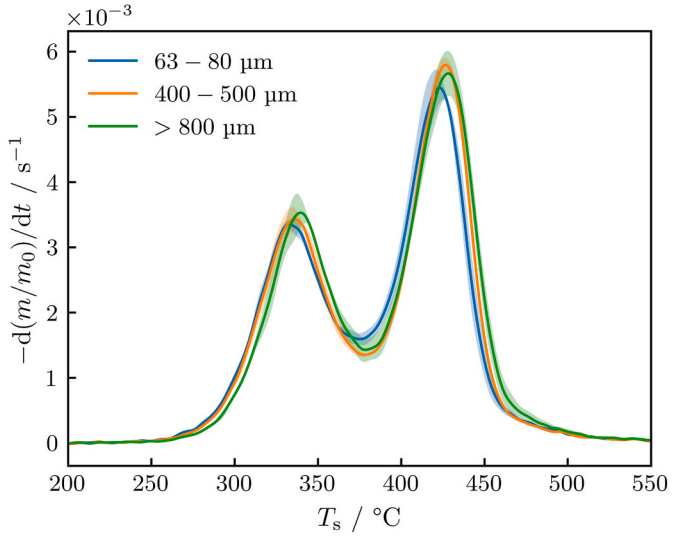

Fig. A.2. dTG results for different particle sizes of polyurethane, showing specimen-form-dependent shifts to higher temperatures. The adequacy of the sample mass was verified by means of mass down-scaling ($\beta = 30\,\mathrm{K\ min^{-1}}$, $m_0 = 1$ mg; solid lines represent the average of three replicates; shaded areas: standard deviation).

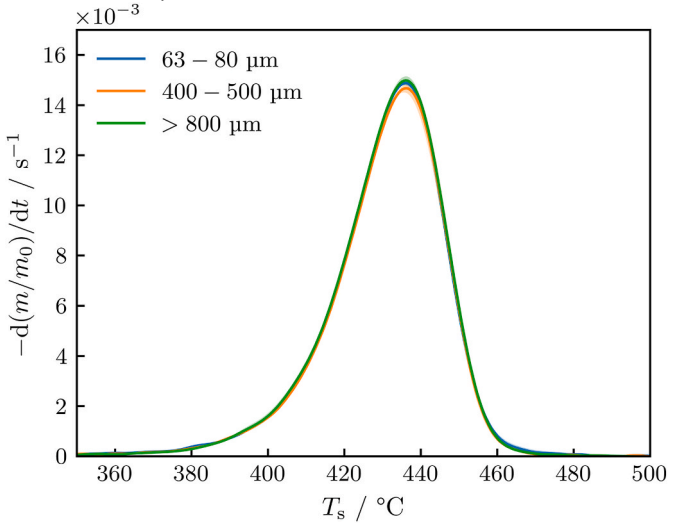

Fig. A.3. dTG results for different particle sizes of polystryrene with no influence of the specimen form. The adequacy of the sample mass was verified by means of mass down-scaling ($\beta = 30\,\mathrm{K\ min^{-1}}$, $m_0 = 1$ mg; solid lines represent the average of three replicates; shaded areas: standard deviation).

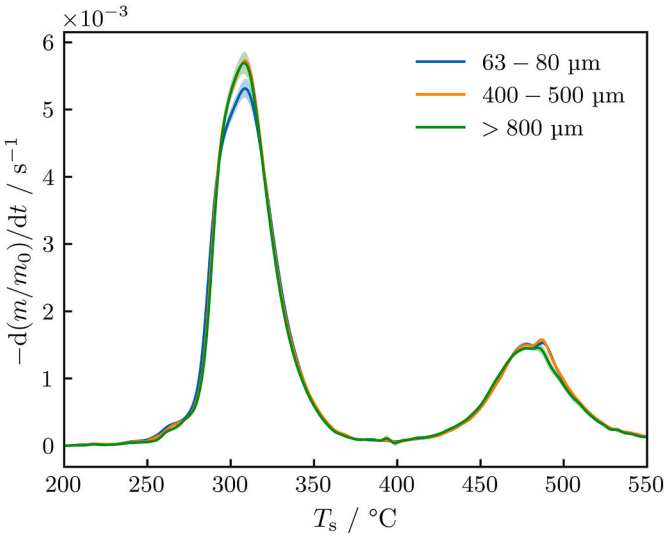

Fig. A.4. dTG results for different particle sizes of polyvinylchlorid with no influence of the specimen form. The adequacy of the sample mass was verified by means of mass down-scaling ($\beta = 30$ K min^{-1}, $m_0 = 1$ mg; solid lines represent the average of three replicates; shaded areas: standard deviation).

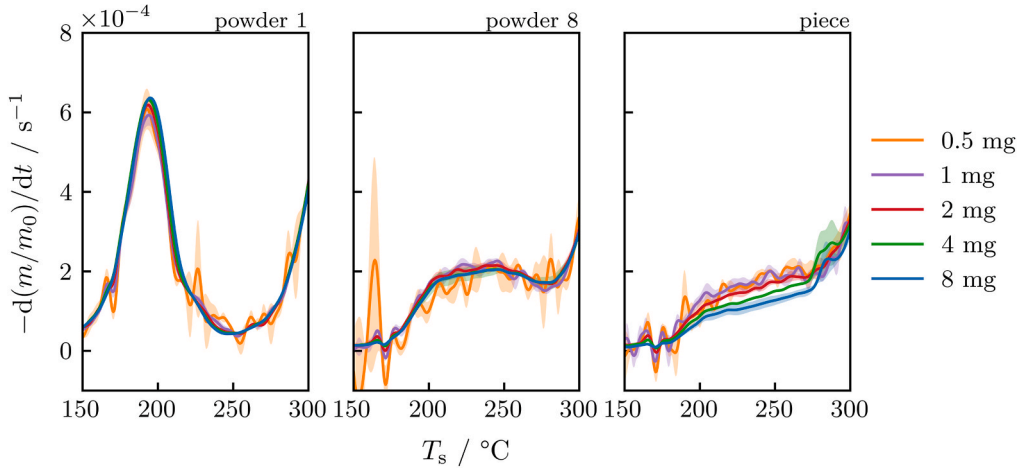

Fig. A.6. dTG signal comparison for the mass down-scaling. Focus on low-temperature range of the decomposition of powder 1, powder 8 and the piece sample at $\beta = 30$ K min^{-1} (solid lines: average; shaded areas: standard deviation).